

## Controlled metal crumpling as an alternative to folding for the fabrication of nanopatterned meta-biomaterials

Ganjian, Mahya; Janbaz, Shahram; van Manen, Teunis; Tümer, Nazli; Modaresifar, Khashayar; Minneboo, Michelle; Fratila-Apachitei, Lidy E.; Zadpoor, Amir A.

**DOI**

[10.1016/j.matdes.2022.110844](https://doi.org/10.1016/j.matdes.2022.110844)

**Publication date**

2022

**Document Version**

Final published version

**Published in**

Materials and Design

**Citation (APA)**

Ganjian, M., Janbaz, S., van Manen, T., Tümer, N., Modaresifar, K., Minneboo, M., Fratila-Apachitei, L. E., & Zadpoor, A. A. (2022). Controlled metal crumpling as an alternative to folding for the fabrication of nanopatterned meta-biomaterials. *Materials and Design*, 220, Article 110844. <https://doi.org/10.1016/j.matdes.2022.110844>

**Important note**

To cite this publication, please use the final published version (if applicable). Please check the document version above.

**Copyright**

Other than for strictly personal use, it is not permitted to download, forward or distribute the text or part of it, without the consent of the author(s) and/or copyright holder(s), unless the work is under an open content license such as Creative Commons.

**Takedown policy**

Please contact us and provide details if you believe this document breaches copyrights. We will remove access to the work immediately and investigate your claim.



Contents lists available at ScienceDirect

## Materials &amp; Design

journal homepage: [www.elsevier.com/locate/matdes](http://www.elsevier.com/locate/matdes)

## Controlled metal crumpling as an alternative to folding for the fabrication of nanopatterned meta-biomaterials



Mahya Ganjian<sup>a,\*</sup>, Shahram Janbaz<sup>a,b</sup>, Teunis van Manen<sup>a</sup>, Nazli Tümer<sup>a</sup>, Khashayar Modaresifar<sup>a</sup>, Michelle Minneboo<sup>a</sup>, Lidy E. Fratila-Apachitei<sup>a</sup>, Amir A. Zadpoor<sup>a</sup>

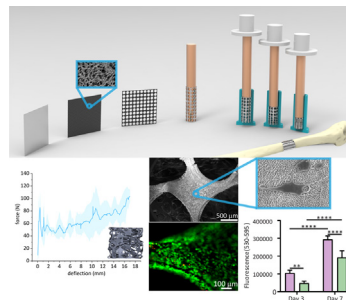
<sup>a</sup> Department of Biomechanical Engineering, Faculty of Mechanical, Maritime, and Materials Engineering, Delft University of Technology, Mekelweg 2, 2628CD Delft, the Netherlands

<sup>b</sup> Institute of Physics, University of Amsterdam, Science Park 904, 1098 XH Amsterdam, the Netherlands

### HIGHLIGHTS

- A novel crumpling approach was developed that allows for the fabrication of 3D metallic nanopatterned scaffolds.
- The fabricated metallic scaffolds have the desired geometrical and tuneable mechanical properties.
- Since the crumpling process starts from a flat state, it is possible to incorporate cell-instructive nanopatterns with arbitrarily complex shapes onto the specimens.
- The response of the MC3T3-E1 preosteoblast cells to the nanopatterned scaffolds was an indicative of the cytocompatibility and potentially an osteogenic behavior.

### GRAPHICAL ABSTRACT



### ARTICLE INFO

#### Article history:

Received 16 February 2022

Revised 9 June 2022

Accepted 10 June 2022

Available online 14 June 2022

#### Keywords:

Crumpling

Bone scaffolds

Orthopedic biomaterials

Cell-nanopattern interactions

2D-to-3D transition

### ABSTRACT

We designed and fabricated a simple setup for the controlled crumpling of nanopatterned, surface-porous flat metallic sheets for the fabrication of volume-porous biomaterials and showed that crumpling can be considered as an efficient alternative to origami-inspired folding. Before crumpling, laser cutting was used to introduce pores to the sheets. We then fabricated titanium (Ti) nanopatterns through reactive ion etching on the polished Ti sheets. Thereafter, nanopatterned porous Ti sheets were crumpled at two deformation velocities (*i.e.*, 2 and 100 mm/min). The compression tests of the scaffolds indicated that the elastic modulus of the specimens vary in the range of 11.8–13.9 MPa. Micro-computed tomography scans and computational simulations of crumpled scaffolds were performed to study the morphological properties of the resulting meta-biomaterials. The porosity and pore size of the scaffolds remained within the range of those reported for trabecular bone. Finally, the *in vitro* cell preosteoblasts culture demonstrated the cytocompatibility of the nanopatterned scaffolds. Moreover, the aspect ratio of the cells residing on the nanopatterned surfaces was found to be significantly higher than those cultured on the control scaffolds, indicating that the nanopatterned surface may have a higher potential for inducing the osteogenic differentiation of the preosteoblasts.

© 2022 The Authors. Published by Elsevier Ltd. This is an open access article under the CC BY-NC-ND license (<http://creativecommons.org/licenses/by-nc-nd/4.0/>).

\* Corresponding author.

E-mail address: [m.ganjian@tudelft.nl](mailto:m.ganjian@tudelft.nl) (M. Ganjian).

## 1 Introduction

One of the major challenges in orthopedic surgery is the treatment of segmental bone defects, as the current clinical solutions are associated with major limitations [1]. Therefore, the quest for ideal bone substitutes that mimic the various properties of the bone is ongoing. Affording synthetic bone substitutes with functionalities that allow them to regulate cell behavior (e.g., cell adhesion, proliferation, and osteogenic differentiation) could greatly increase their chance of successful osseointegration. For instance, it is well known that the behavior of cells is affected by the physical [2–4], mechanical [5–9], and geometrical [10] properties of their environment. For instance, cell proliferation, migration, and differentiation can be affected by the physical cues in the environment, including stiffness [11,12], viscoelasticity [13], and submicron/nano topographies [2,3] of the substrate they reside on. Moreover, it is now understood that the three-dimensional (3D) shape of the environment at a larger scale can also regulate stem cell behavior [10].

The introduction of nanotopographies to the surface of bone substitutes is particularly appealing, because well-designed surface ornaments may be able to (simultaneously) kill bacteria [3,14–19] and induce osteogenesis [2,16,20]. In this regard, introducing holes to the flat sheet not only regulates the mechanical properties of such 3D structures but could also address the morphology-based aspects that are required for bone tissue regeneration, such as suitable mass transport properties for the transportation of oxygen, nutrients, and metabolites [21] and cell settlement. Moreover, as the mechanical properties of metallic implants are generally higher than those of the native bone, introducing pores into scaffolds is beneficial for adjusting the mechanical properties of the implants such that they fall within the range of the mechanical properties reported for the human bone [22–24]. Nowadays, most 3D lattice structures are manufactured using additive manufacturing (AM, = 3D printed) techniques. Given the fact that most of the micro/nano-patterning techniques work only on flat surfaces, they cannot be easily applied to porous meta-biomaterials whose surface areas are primarily internal and non-planar (i.e., 3D) [3]. Several techniques have been, therefore, proposed to start from an initially flat sheet, decorate the surface with nanopatterns, and transform the flat construct to a 3D object through crumpling [25], origami [26,27], or kirigami [28,29]. As opposed to origami and kirigami that tend to create regular and precise geometries, crumpling introduces random geometric configurations and creases, leading to 3D structures that are less sensitive to geometric and topological imperfections [25].

The morphologies of mammalian brain cortex [30,31], DNA packaging in viral capsids [32], flower or plant leaves in buds [33], the wing folding of insects in cocoons [34], and the confinement of chromatin in the nucleus of a cell [35,36] are all examples of naturally occurring crumpled objects. In addition to replicating such structures, crumpling provides an opportunity to create unusual combinations of material properties that are rarely found in nature [25,37].

Well-designed flat thin sheets crumpled under controlled conditions may be used to create crumpling-based metamaterials [37]. To date, many different techniques have been employed to crumple thin sheets, including hand crumpling [25], distributing a net of wires around loosely crumpled thin sheet [37], leaving the loosely crumpled specimen at ambient pressure [38], and using a cylindrical die [33–42]. While hand crumpling is considered the easiest and the most commonly used method, it suffers from irreproducibility and uncontrollability. Moreover, measuring the applied force is not feasible in this method [25]. Crumpling using a die is a controlled technique that enables the measurement of the applied force and the level of compaction [25]. It is, therefore,

a promising candidate for the fabrication of meta-biomaterials. Nevertheless, no such applications of controlled crumpling for the fabrication of meta-biomaterials have been previously demonstrated.

Here, we present a novel class of meta-biomaterials that combine controlled crumpling with surface nanopatterns and laser-cut surface porosities. We used a cylindrical die to crumple laser-cut porous Ti sheets that were first nanopatterned with inductively coupled plasma reactive ion etching (ICP RIE) to create black titanium (bTi) [14] (Fig. 1a). To protect the nanopatterns during the crumpling process, the sheets were coated with a thin layer of polyvinyl alcohol (PVA). The mechanical properties of the crumpled structures were measured using mechanical testing, while their morphological properties were determined using micro-computed tomography ( $\mu$ CT). Moreover, the finite element method (FEM) was used to simulate the crumpling process. Furthermore, we investigated the cytocompatibility of the nanopatterned specimens using *in vitro* cell culture assays (i.e., live/dead, metabolic activity) and scanning electron microscopy (SEM), respectively.

## 2. Results

### 2.1. Laser cutting

The STL files describing the geometry of the flat specimens were imported into the laser machine and were used to cut through the 4-inch titanium foil (Fig. 1c). The damage inflicted to the sheet by the cutting process was limited to a radius of  $\sim 120$   $\mu$ m away from the laser beam (Fig. 1d).

### 2.2. Fabrication and characterization of the bTi nanopatterns

The desired nanopatterns that are characteristic of bTi were formed on the surface of the Ti sheets (Fig. 1e). After crumpling and the removal of the PVA layer, the bTi nanopatterns were analyzed using SEM (Fig. 1f–h). The nanopatterns (Fig. 1g) and the micro-features formed on the surface during the laser cutting process (Fig. 1h) were fully preserved and remained intact during the crumpling process.

While the water contact angle of the flat Ti surface was approximately  $75^\circ$  (Fig. 1b), the black Ti surfaces were super hydrophilic with a water contact angle  $< 6.0^\circ$  (Fig. 1b).

Furthermore, the atomic force microscopy (AFM) measurements of the black Ti surfaces revealed an average surface roughness of  $R_a = 157 \pm 6$  nm.

### 2.3. Compression tests

The force–deflection curves were typical for porous biomaterials [43] including such characteristic features as an initially linear increase in deflection with force, a relatively long plateau region with fluctuations, followed by a compaction region where stress rapidly increased (Fig. 2a). The peaks and valleys in the force–deflection curves (Fig. 2a) were caused by the formation of shear lines (Fig. 2c and d) and the build-up of the stress after the load was transferred to neighboring layers.

Regardless of the deformation velocity, the specimens with the lowest surface porosity (i.e., 48.0%) required relatively higher compression forces to reach the same deformation than the specimens with the surface porosities of 52.5% and 57.2% (Fig. 2a). Even though a higher rate of deformation (i.e., 100 mm/min) did not increase the force needed to reach the same level of compaction, it decreased the standard deviation of the applied force (Fig. 2a).

In the case of a lower deformation velocity and for the specimens with a surface porosity of 57.2%, two layers of Ti sheets

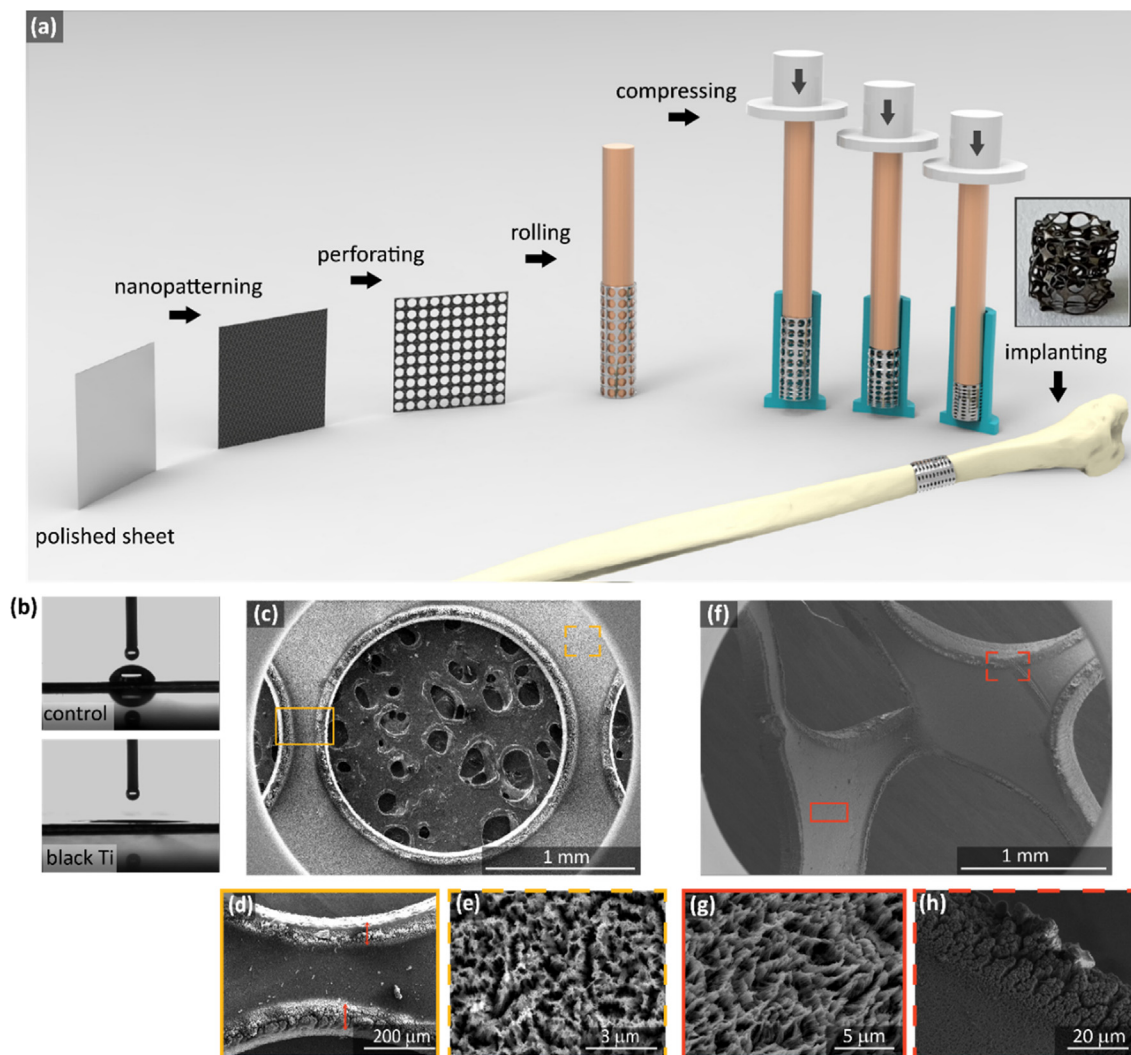


**Fig. 1.** (a) A schematic illustration of the steps involved in the crumpling of nanopatterned porous Ti sheets. (b) A Water droplet residing on the control and black Ti surface after 5 s. (c) A low-magnification SEM image of a laser-cut pore on the surface of a Ti sheet. (d) A low-magnification SEM image of the nanopatterned Ti sheet shows that the laser beam affects the nanopatterns within a 60–120  $\mu\text{m}$  radius. (e) A high-magnification SEM image of the bTi nanopatterns far away from the laser beam. Nanopatterns with a distance that was  $>120 \mu\text{m}$  had a normal morphology and remained intact. (f) A low-magnification SEM image of the crumpled scaffold. A high-magnification SEM image of (g) the bTi nanopatterns on the Ti sheet after crumpling process and (h) the undesired artifacts created during the laser cutting process after crumpling.

enhanced the mechanical properties of the crumpled structure and up to 112% higher forces were required to compress them as compared to the single-layer specimens (Fig. 2b).

The force–displacement curves corresponding to all the crumpled specimens suggest that the strengths of the crumpled structures remain almost constant as the level of compaction increases. At the same time, their strength is determined according to the geometrical design of the flat material (Fig. 2a and b).

#### 2.4. FEA and $\mu\text{CT}$

The top and side views of the 3D scanned and simulated samples confirmed that changing the deformation velocity from 2 mm/min to 100 mm/min did not alter the general morphology of the final scaffolds (Fig. 2c and d). Given the fact that the specimens were rolled around a cylindrical bar and were confined in a die (Fig. 1a), the final morphology of the  $\mu\text{CT}$ -imaged specimens was more cylindrical.

Crumpling the Ti sheets with the surface porosities of 48.0%, 52.5%, and 57.2% with a deformation velocity of 2 mm/min resulted in the volume porosities of  $87.6 \pm 2.8\%$ ,  $89.1 \pm 1.6\%$ , and  $89.7 \pm 3.5\%$  for the crumpled scaffolds, respectively (Table 1). By

increasing the deformation velocity to 100 mm/min, the volume porosities changed to  $87.6 \pm 2.8\%$ ,  $88.7 \pm 3.8\%$ , and  $90.4 \pm 2.9\%$ , respectively (Table 1). The results of the FEA simulations were in line with those of the experiments (Table 1), indicating that while increasing the surface porosity of the sheets slightly increased the volume porosity of the crumpled scaffolds, the changes in the volume-porosity were relatively small.

The porosity, trabecular thickness, and pore size values were uniformly distributed throughout the scaffolds (Fig. 3a–c) except for the specimens with surface porosities of 48.0% and 52.5% and crumpled with a deformation velocity of 2 mm/min for which there was a significant difference between the porosity values of two different segments along the length of the scaffolds (Fig. 3a).

Although the trabecular thickness values were uniformly distributed along the length of the scaffold and there was no significant difference between the different segments, the values resulting from the FEA simulations were relatively higher than those obtained experimentally (Fig. 3b).

In the FEA simulations, there was a significant difference between the pore size values calculated for two different segments of the specimens with a surface porosity of 48.0% that were crumpled at 2 mm/min. For the other specimens, there was no signifi-

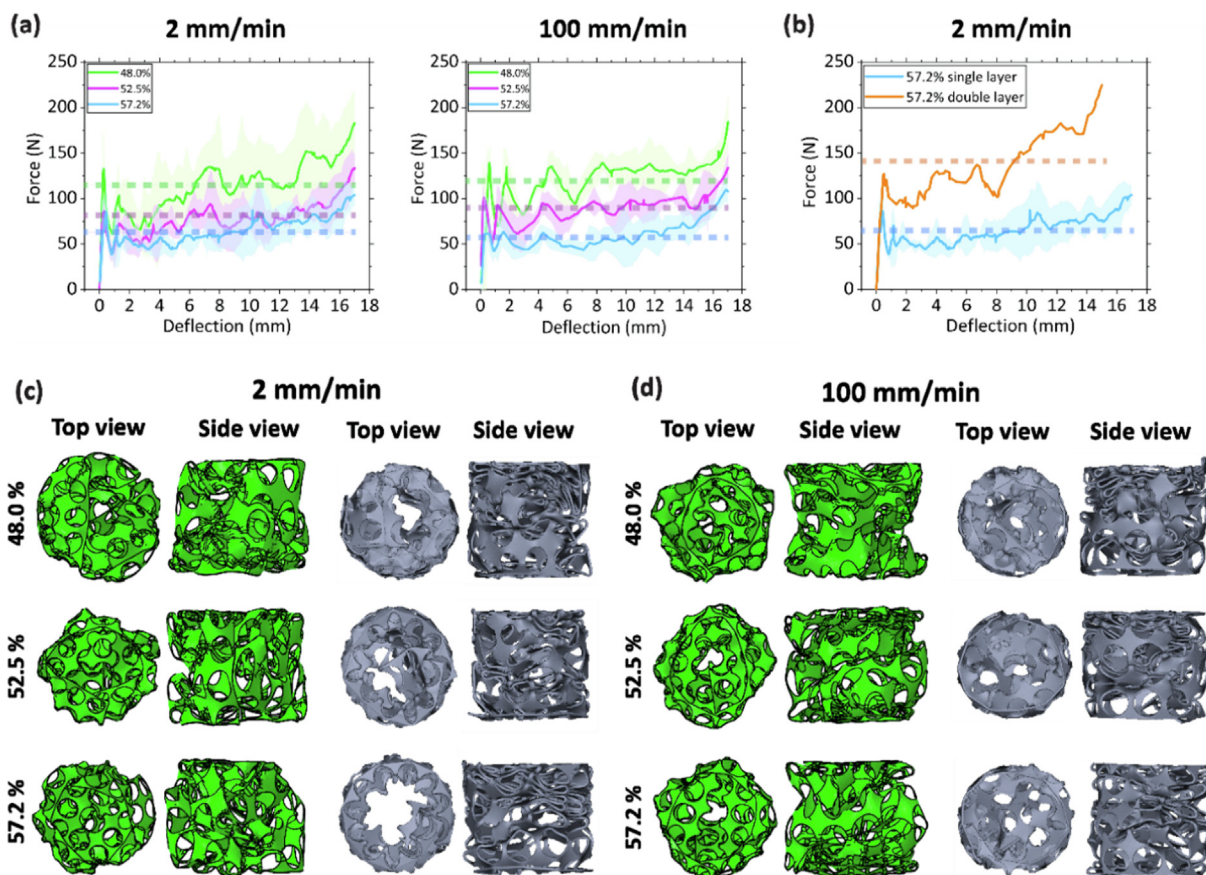


**Fig. 2.** (a) The force–deflection curves recorded during the crumpling process for the Ti sheets ( $n = 3$ ) with three levels of surface porosity and crumpled using different deformation velocities of 2 mm/min and 100 mm/min. The straight lines represent the results of the experiments and while the hatched area represents the standard deviation for three different specimens. The dashed lines represent the mean strength of the crumpled scaffolds as a function of the pore size. (b) The force–deflection curves of the single- and double-layer porous Ti sheets, crumpled using a deformation velocity of 2 mm/min. The top and side views of the crumpled specimens resulting from the FEA simulations and  $\mu$ CT imaging for the deformation velocities of (c) 2 mm/min and (d) 100 mm/min.

**Table 1**  
Morphological characteristic of the different types of porous scaffolds.

Deformation velocity (mm/min)	Flat specimen Surface porosity (%)	3D scaffold											
		Volume Porosity $\phi$ (%)				Sheet thickness (Tb.Th) ( $\mu$ m)				Pore size (Tb.Sp) ( $\mu$ m)			
		$\mu$ CT	SD	FEA model	SD	$\mu$ CT	SD	FEA model	SD	$\mu$ CT	SD	FEA model	SD
2	48.0	87.6	2.8	88.6	0.7	144.8	4.4	211.7	3.1	581.3	34.6	520.4	3.1
	52.5	89.1	1.6	89.7	0.5	146.3	5.7	214.5	2.8	594.1	26.7	525.0	2.8
	57.2	89.7	3.5	90.7	0.3	147.9	5.8	214.4	1.5	603.5	38.8	534.0	1.2
100	48.0	87.6	2.8	88.1	1.6	142.8	2.5	211.5	3.0	578.6	38.4	517.9	2.4
	52.5	88.7	3.8	89.7	1.5	147.1	5.7	207.6	2.7	590.7	53.4	537.3	2.5
	57.2	90.4	2.9	90.0	1.0	145.6	4.5	218.6	3.7	606.1	39.9	521.4	3.7

Tb.Th. trabecular thickness, Tb. Sp., trabecular spacing (*i.e.*, pore size).

cant difference between the pore size values corresponding to the different segments along the length of the crumpled specimens (Fig. 3c).

### 2.5. Mechanical properties of the scaffolds

There was no significant difference between the elastic modulus of the scaffolds fabricated using three different values of surface porosities crumpled at two different deformation rates (Fig. 3d). For all experimental groups, the  $E$  modulus remained in the range of 11.8 MPa (for a surface porosity of 57.2% crumpled at 100 mm/min) to 13.9 MPa (for a surface porosity of 52.5% crumpled at 2 mm/min) (Table 2). However, there was a lower degree of

variation in the elastic moduli of the specimens crumpled at a higher deformation velocity (*i.e.*, 100 mm/min) (Fig. 3d and Table 2).

The percentage of the elastic recovery remained in the range of 3.62% to 4.60% for all of the crumpled specimens, with no significant variation between the different groups (Table 2).

### 2.6. Cytocompatibility of un-crumpled scaffolds

At day 7, the vast majority of the cells were found to be viable on both polished and nanopatterned un-crumpled specimens (Fig. 4a). Moreover, the cells were uniformly distributed on both types of the specimens (Fig. 4a and b) and had a normal morphol-

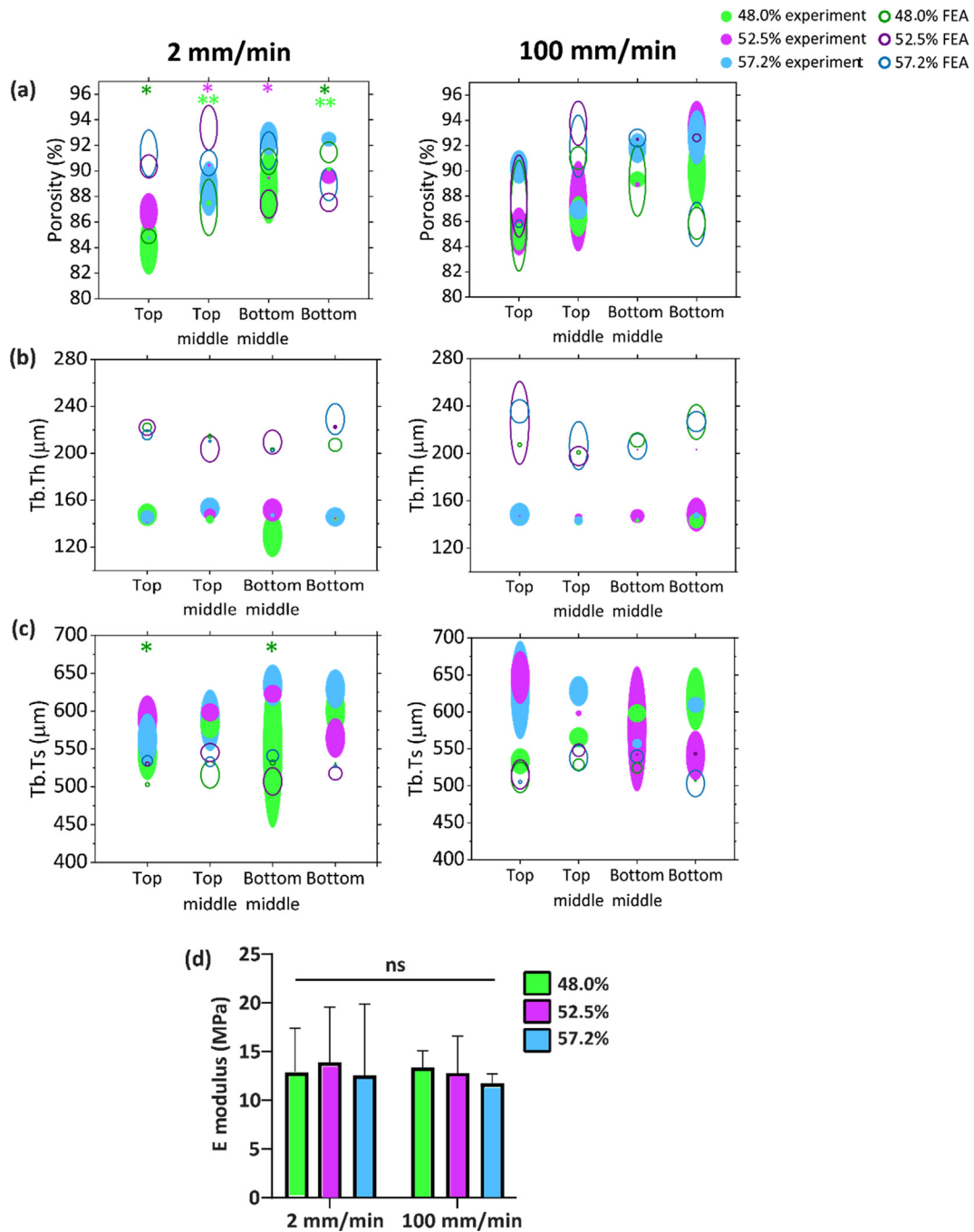


**Fig. 3.** The distribution of the (a) porosity, (b) trabecular thickness, and (c) pore size for the specimens with different surface porosities that were crumpled using different deformation velocities ( $n = 3$ ). The greater oval diameter indicates the standard deviation of the corresponding values (\* $p < 0.05$  and \*\* $p < 0.01$ ). (d) The elastic modulus of the scaffolds with different porosities crumpled using different deformation velocities ( $n = 3$ ).

**Table 2**  
The elastic modulus ( $E$ ) and elastic recovery of the scaffolds.

Deformation velocity (mm/min)	Surface porosity (%)	$E$ (MPa)		Elastic recovery (%)	
		Avg	SD	Avg	SD
2	48.0	12.9	4.5	3.92	0.33
	52.5	13.9	5.7	3.92	1.11
	57.2	12.6	7.3	3.62	1.11
100	48.0	13.4	1.7	4.31	1.95
	52.5	12.8	3.8	4.41	1.24
	57.2	11.8	0.9	4.60	2.53

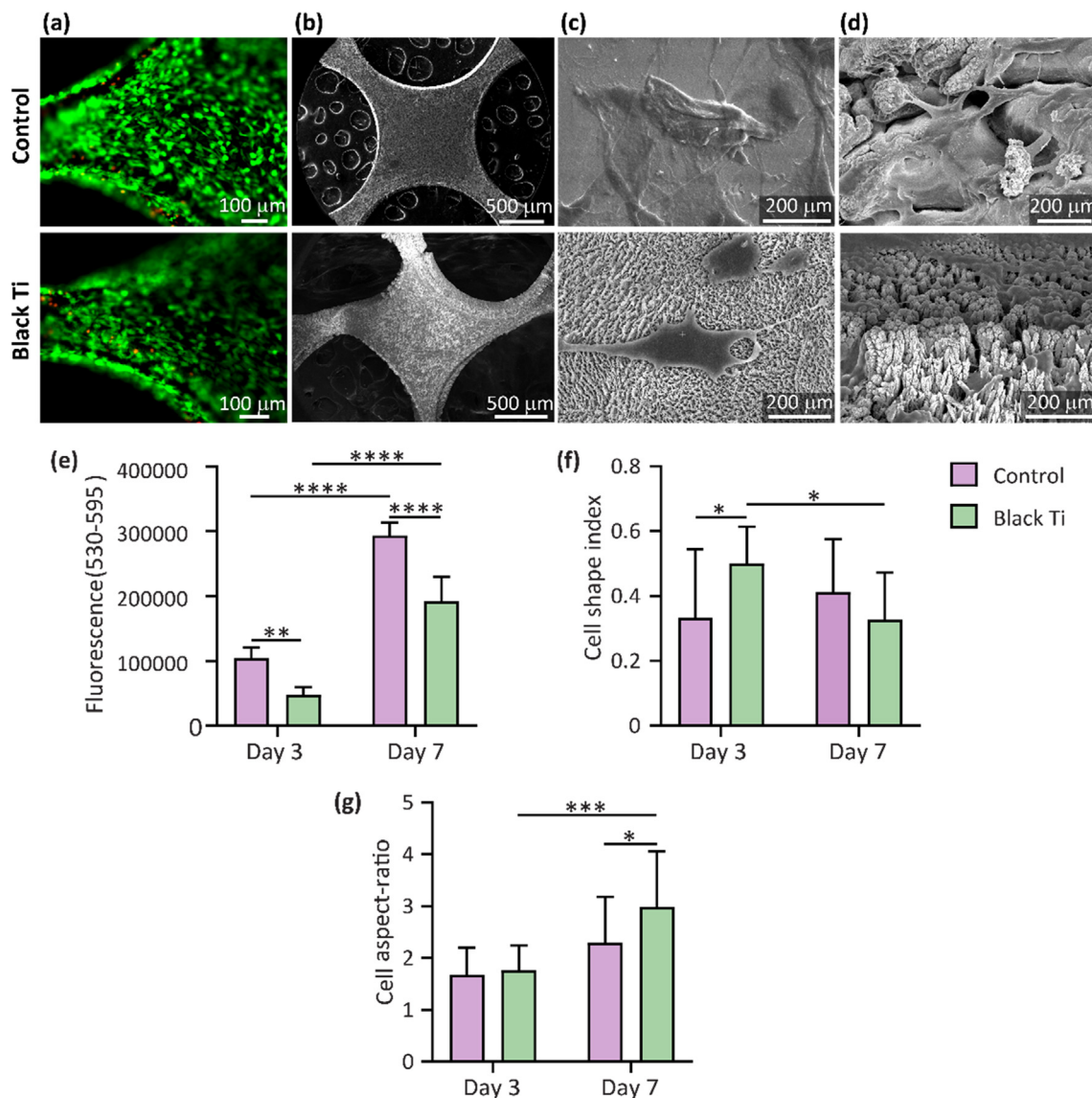


**Fig. 4.** (a) Live/dead staining and (b) SEM imaging of the MC3T3-E1 cells after 7 days of culture on the control and nanopatterned un-crumpled specimens. High magnification SEM images (day 7) of the MC3T3-E1 cells residing on (c) the control and nanopatterned un-crumpled specimens and (d) on the laser cutting artifacts. (e) The metabolic activity (day 7) of the preosteoblast cells cultured on the control and nanopatterned un-crumpled specimens measured through the PrestoBlue assay. (f) Shape index and (g) aspect ratio of the MC3T3-E1 preosteoblast cells on the surface of the control and nanopatterned un-crumpled specimens after 3 and 7 days of culture (\* $p < 0.05$  and \*\*  $p < 0.01$ , \*\*\*  $p < 0.001$ , \*\*\*\*  $p < 0.001$ ).

ogy (Fig. 4c). Furthermore, there was no indication that the artifacts created during the cutting procedure had affected cell viability (Fig. 4a, d).

### 2.7. Metabolic activity and morphological characteristics of cells

The metabolic activity of the cells seeded on the polished scaffolds was significantly higher than those cultured on the nanopatterned surfaces on both days 3 and 7. For each experimental group analyzed separately, the metabolic activity of the cells significantly increased with time (Fig. 4e). The cells residing on the nanopatterned scaffolds were more rounded as compared to the cells cultured on the polished scaffolds after 3 days of culture (Fig. 4f). After 7 days, however, the cell shape index on the nanopatterned scaffolds significantly decreased (Fig. 4f). Similarly, while the cell aspect ratio was not significantly different between the surfaces after 3 days, the cells were more elongated after 7 days on the nanopatterned scaffolds. In addition, a significant change in the cell

aspect ratio between 3 and 7 days was only observed on the nanopatterned scaffolds (Fig. 4g).

### 3. Discussion

In this study, for the first time, an efficient crumpling technique was proposed to fabricate porous 3D metallic scaffolds from initially flat nanopatterned sheets. Crumpling is an interesting alternative to origami and kirigami approaches as it greatly simplifies the process of going from a flat construct to a 3D porous structure. Given the stochastic nature of the crease patterns and folding sequences, the resulting structure is highly resistant to minor imperfections, while highly regular origami/kirigami lattices are very sensitive to the slightest deviations from the perfect geometry. Moreover, controlled crumpling offers a high degree of tunability in terms of mechanical properties and morphological features. For example, the porosity and pore size of the final 3D scaffold can be tuned by adjusting the geometrical features of surface por-

ous sheet and the level of compaction during the crumpling process.

Within the context of meta-biomaterials, nano/micro-patterned 3D structures that guide stem cells along the desired pathway of differentiation are essential [44,45]. The 3D geometry of the biomaterials used in bone tissue engineering, including their porosity and pore size, are crucial factors determining the biological response of these materials elicit upon implantation [46]. A proper choice of the porosity, pore size, pore shape, and pore distribution facilitates cell oxygenation, migration, spreading, settlement, and feeding (*i.e.*, transportation of metabolites and nutrients) [1,46–48]. The same morphological parameters also affect the mechanical properties of the scaffolds [1]. Even though highly porous scaffolds increase the potential for bone ingrowth, they generally offer limited mechanical performance [46]. The porosity of bone tissue engineering scaffolds should, therefore, be chosen such that the conflicting biological and mechanical requirements are simultaneously satisfied. The native bony tissue has different porosity values depending on its type (*i.e.*, cortical or trabecular). For instance, cortical bone (compact bone) has a relatively dense structure (porosity = 5–25%) with longitudinally cylindrical elements, while trabecular (spongy) bone has a highly porous structure (porosity = 40–95%) with a network of trabeculae [46,49]. However, native bone is highly vascularized, meaning that higher porosities are likely to be needed at the beginning of the tissue regeneration process where mass transport should occur through diffusion. Porosities > 60% are suggested to be suitable for bone scaffolds [49]. All the experimental groups in this study had volume porosities that were within this suggested range.

As for the pore size, the suggested range is 300–900  $\mu\text{m}$  [49]. Similar to the porosity, all the six experimental groups considered here satisfied this requirement as well (Table 1). According to the results of  $\mu\text{CT}$  imaging and FEA simulations, increasing the deformation velocity did not influence the morphology, volume porosity, trabecular thickness, and pore size of the final scaffold, which means that a higher deformation velocity (*i.e.*, 100 mm/min) can be applied to speed up the process and enhance the throughput. In the simulations, the surface-porous sheets were rolled with the same diameter as that of the bar. However, they were not confined in a cylindrical die. This can explain the differences observed between the final morphology of the scaffolds resulted from the simulations and experiments (Fig. 2c and d). Moreover, at the higher deformation velocity, less deviations from the average values of the morphological properties were observed (Fig. 3a–c), suggesting that a higher rate of deformation leads to a more uniform crumpled structure.

The differences between the trabecular thickness of the  $\mu\text{CT}$  scanned samples and those obtained computationally (Fig. 3b) can be explained by the process used for converting the simulation results from a geometry based on shell elements to a geometry based on solid elements. Although a uniform thickness of 125  $\mu\text{m}$  was assigned to the shell-based structure, the thickness slightly (*i.e.*, by approximately + 14  $\mu\text{m}$ ) increased after applying the wrapping operation that was used to protect thin walls from collapsing.

While the mechanical properties of the specimens are lower than the human bone (Table 2), it is important to realize that the mechanical properties of such scaffolds can be tuned by changing the porosity, pore size, thickness of the initial flat sheet, or by using multi-layers of Ti sheets instead of a single layer. Using multiple stacked sheets for crumpling results in a higher degree of structural integrity and higher values of the scaffold stiffness. Moreover, the forces required for reaching the same level of crumpling increase when multiple stacked sheets are used (Fig. 2b). Furthermore, the desired mechanical properties of the bone scaffolds depend on the implantation site and whether or not it is load-

bearing. For instance, higher mechanical properties are required for the treatment of load-bearing bones of the lower extremity, as the implant needs to be able to endure the weight of the body for 12–24 weeks (bone healing process). In other cases, such as cranial defects and some of the upper limb implants (*e.g.*, fingers), the loads tend to be much smaller and the total timespan may be shorter (*e.g.*, 3–12 weeks [50]). In principle, there are implant types in which the implant is surrounded by a bony environment that protects its integrity. An example of such implants is the implants used for the treatment of acetabular defects where the surrounding bony tissue stabilizes the crumpled scaffold and protects them against uncrumpling. Moreover, bone substitutes are often loaded under compression in which case the risk of uncrumpling is relatively small. Finally, bony ingrowth into crumpled implants may interlock the crumpled structure, thereby improving their stability. A different choice of material and a thicker layer of the Ti sheets could also increase the mechanical properties of the scaffold. However, thicker metal sheets are less bendable [51].

It has been demonstrated that nanotopographical features on the surface of biomaterials can significantly influence the cell behavior [2]. One of the major challenges associated with controlled crumpling is to protect the nanopatterns from being damaged during the crumpling process. The PVA layer coated on the surface of nanopatterned scaffolds was successful in fully protecting the applied nanopatterns. The live/dead, cell metabolic activity assays, and SEM imaging showed that the preosteoblasts can survive and proliferate after adhesion to the uncrumpled scaffolds. Similar bTi nanopatterns formed on the surface of a flat Ti sheet have been previously shown to support cell adhesion and proliferation [3]. However, the cells were metabolically less active on bTi surfaces as compared to flat Ti. Similar observations have been made in previous studies [3] and suggest that the effects of the different adaptation of cells to bTi nanopatterns go beyond morphological changes and involve cell metabolism. It has been shown that surface nanotopography affects the molecular diffusion through the cell plasma membrane [52] and furthermore, cell mechanics and metabolism are mutually related [53]. Therefore, further dedicated metabolic studies are required to understand why cells may show lower levels of metabolic activity when cultured on nanopatterned structures. The laser-cutting artifacts and the ridges created during the crumpling process did not adversely affect the cell response. Previous studies have been shown that bTi nanopatterns applied to flat Ti sheet are capable of killing bacteria via mechanical interactions [3,14] and of increasing matrix mineralization [3] by preosteoblasts. Furthermore, elongated cell morphology is considered beneficial for osteogenic commitment [3,54–57]. After 7 days, we observed a significant increase in the elongation of the cells residing on the nanopatterned scaffolds (Fig. 4g). The measured values of the cell shape index and aspect ratio indicate that the cells attached to the nanopatterned scaffolds have a greater tendency to transform from an initial rounded shape to an elongated and polarized morphology as compared to the cells attached to the polished specimens (Fig. 4f and g). The exact mechanisms through which the cells undergo morphological changes upon interactions with surface nanopatterns have not been fully understood yet. Several studies have further investigated such effects and have attributed them to changes in the size and distribution of focal adhesions [3,54]. As the formation of focal adhesions is largely a force-dependent process, traction force microscopy and the measurement of the adhesion force between the cells and nanopatterned substrate are necessary to answer this question. It can be speculated that forces generated by cells attached to the nanopatterns might affect the cytoskeletal organization and eventually, cell shape. The transduction of forces to the cell nucleus might also affect the transcriptional factors, such as YAP, that is shown to regulate the cell shape [58]. It is also note-

worthy that the semi-crumpled structures and the fact that only one side of the initial 2D sheet is nanopatterned make it extremely challenging to perform certain *in vitro* assays such as immunocytochemical staining, assessment of mineralization, and qPCR. Therefore, to reveal the ultimate potential of these structures for regenerating bone, we would recommend *in vivo* studies as the best approach for future research.

Due to the lack of any systematic studies, it is difficult to draw a conclusion on how surface roughness modulates cell behavior [59]. Cai *et al.*, assessed the effects of surface roughness of Ti films on osteoblast proliferation. They showed that increasing the surface roughness from  $1.94 \text{ nm} \pm 0.24 \text{ nm}$  to  $10.27 \pm 0.45 \text{ nm}$  and  $20.73 \pm 2.68 \text{ nm}$  had only minor effect on the proliferation of osteoblasts [60]. Khang *et al.*, cultured mesenchymal stem cells (MSCs) on three different Ti surfaces with 0.645, 3.85, and 13.37 nm as the roughness values. They reported that cell adhesion and fibronectin adsorption increased with the surface roughness [61]. In another study, Hou *et al.*, systematically tuned the average roughness ( $R_a$ ) of Ti surface from nano- to micro-scales (53.86 to 1050.31 nm) [59]. They observed that the densest and longest filopodia were formed on the surface with an intermediate roughness value (*i.e.*,  $R_a = 278.64 \text{ nm}$ ). Interestingly, this roughness value was the one that highly enhanced the formation of FAs as well as the osteogenic differentiation of cells. The mean values of the surface roughness measured in our study are relatively close to the optimum values reported in their study. Nevertheless, since a similar average surface roughness may be generated by different surface morphologies, both should be considered for understanding and comparing cell responses.

It is worth mentioning that we only functionalized one side of the scaffolds. The nanopatterning process may deliver more impact when the surface functionalization is applied to both sides of the sheet. Based on the results reported here, controlled crumpling is a promising approach for the fabrication of 3D porous bone scaffolds decorated with surface nanopatterns. Further research is, therefore, required to more thoroughly elucidate the potential of these porous meta-biomaterials.

#### 4. Conclusions

To address the limitations of the existing techniques for the production of nanopatterned meta-biomaterials, a novel crumpling approach was developed that allows for the fabrication of 3D metallic scaffolds with the desired size, volume porosity, and mechanical properties from nanopatterned surface-porous sheets. Since the crumpling process starts from a flat state, it is possible to incorporate nanopatterns with arbitrarily complex shapes onto the specimens. The nanopatterns were protected and remained intact during the crumpling process. Three different surface porosities of 48.0%, 52.5%, and 57.2% led to three different volume porosities of 87.6%, 89.1%, and 89.7% after crumpling with a rate of 2 mm/min, and 87.6%, 88.7%, and 90.4% after crumpling with a rate of 100 mm/min, meaning that the final porosity can be controlled through the rational design of the flat construct. The porosity, pore size, and trabecular thickness of the final scaffolds fabricated in this study were in the appropriate range for bone scaffolds. According to the  $\mu$ CT and FEA results, the deformation velocity did not significantly affect the morphological and mechanical properties of the final scaffolds. We also designed a double-layer structure to improve the mechanical properties of the crumpled scaffold. Finally, the response of the MC3T3-E1 preosteoblast cells to the nanopatterned scaffolds was generally indicative of high degrees of cytocompatibility and potentially also an osteogenic behavior. The presented controlled crumpling approach, therefore, constitutes a promising route for the realization of nanopatterned

meta-biomaterials with tunable dimensions, porosities, and mechanical properties. Future studies should further evaluate the *in vitro* and *in vivo* performance of these biomaterials, paving the way for their ultimate clinical adoption.

#### 5. Materials and methods

##### 5.1. Sample preparation

Annealed Ti sheets with a thickness of 125  $\mu\text{m}$  were used for this study (99.96% purity, Goodfellow, Huntingdon, UK). The sheets were cut to the size of a 4-inch (diameter = 10.16 cm) silicon wafer and were polished by chemical mechanical polishing (CMP Meca-pol E460, Saint-Martin-le-Vinoux, France). Following this step, the 4-inch titanium sheets were cut into  $22.5 \times 22.5 \text{ mm}^2$  pieces using a laser micromachine (Optec Laser Systems, Belgium).

##### 5.2. Fabrication and characterization of bTi samples

The black Ti nanopatterns were fabricated on the polished Ti specimens using an ICP RIE machine (PlasmaLab System 100, Oxford Instruments, UK). The Ti specimens were glued with a thermal joint compound (type 120, Wakefield Engineering, USA) to a 4-inch fused silica carrier wafer.  $\text{Cl}_2$  and Ar were the etching gasses. The etching process was performed under the following condition: ICP power = 600 W, RF power = 100 W,  $\text{Cl}_2$  flow rate = 30 sccm, Ar flow rate = 2.5 sccm, chamber pressure = 0.02 mbar, temperature = 40 °C, and etching time = 10 min. Following the etching process, the specimens were cleaned in acetone, ethanol, and isopropyl alcohol (IPA) (consecutive steps of 30 min each), and were then spin-dried. High-resolution scanning electron microscopy (SEM) images were taken with a Helios (FEI Helios G4 CX dual-beam workstation, Hillsborough, OR, USA) microscope at 10 kV and 43 pA.

The wettability of the bTi and control surfaces was evaluated by measuring the static water contact angle in duplicate using a drop shape analyzer (DSA 100, Kruss, Germany). A volume of 1.5  $\mu\text{l}$  deionized water with a falling rate of 60  $\mu\text{l}/\text{min}$  was rested on the surface using a syringe. The images were recorded after 5 s.

The mean roughness ( $R_a$ ) of the black Ti surfaces was also estimated as the mean  $\pm$  SD of the values measured for three images of 100  $\mu\text{m}^2$  each by AFM (JPK Nanowizard 4, Bruker, Germany) in the tapping mode, using a high aspect ratio probe (TESPA-HAR, Bruker, Germany) [3].

##### 5.3. Design and manufacturing of the surface-porous flat sheets

The size of the 2D flat sheet ( $22.5 \times 22.5 \text{ mm}^2$ ), the number of the pores per specimen ( $12 \times 12$ ), and the center-to-center inter-spacing (1.875 mm) of the pores were kept constant while the diameter of the pores was varied (1.46 mm, 1.53 mm, and 1.59 mm) using CAD software (Solidworks 2019, Dassault Systèmes). The designs of the flat specimens with three different surface porosities (*i.e.*, 48.0 %, 52.5 %, and 57.2 %) were exported to the laser micromachining in the STL format. In total, 18 specimens were laser cut from non-polished Ti sheets (for mechanical testing) while three specimens were laser cut from the polished Ti sheets (for nanopatterning and cell culture). The laser parameters were as follow: frequency = 50 kHz, diode current = 4 A, laser firing rate = 30 kHz, and the number of repetitions = 40. Consequently, the samples were cleaned in acetone, ethanol, and IPA (consecutive steps of 30 min each), and were spin-dried.

## 5.4. Mechanical experiments

### 5.4.1. Design of the crumpling setup

To crumple the surface-porous Ti sheets, a cylindrical die was fabricated with a fused deposition modeling (FDM) 3D printer (Ultimaker 2+, Ultimaker, The Netherlands), polylactic acid (PLA) filaments, and a 0.25 mm nozzle. Prior to crumpling, the Ti sheets were pre-rolled into a cylindrical shape around a stainless-steel bar ( $d = 7.2$  mm) (Fig. 1a).

### 5.4.2. Compression tests

The crumpling process (Fig. 1a) was carried out using a universal mechanical testing bench (Plus/Lloyd Instruments Ltd, England) equipped with a 5 kN load cell. Before compressing the pre-rolled sheets, the specimens were coated two times with PVA (Resin Technology, France), each step followed by thermal treatment at 50 °C for one hour. The specimens were then placed inside the die and were compressed using the same stainless-steel bar, which was attached to the universal test bench. Two different compression velocities of 2 mm/min and 100 mm/min were applied to study the effects of deformation velocity.

**5.4.2.1. Single-layer specimens.** The single-layer specimens were compressed with a compression velocity of 2 mm/min (three unpolished specimens for each group of surface porosity) and at a compression velocity of 100 mm/min (three unpolished specimens for each group of surface porosity). The tests were continued until a cross-head displacement of 17 mm was reached (initial length = 22.5 mm). In the case of the cell culture specimens, three polished specimens and three nanopatterned specimens, with a surface porosity of 57.2% were crumpled at a velocity of 2 mm/min.

**5.4.2.2. Double-layer specimens.** The double-layer scaffolds were also created by placing two specimens with the same porosity (i.e., 57.2%) on top of each other, rolling them, and placing them into the PLA die. The two-layer specimens were then compressed with a velocity of 2 mm/min. To prevent the scaffolds from being damaged, the test was continued until a cross-head displacement of 15 mm was reached.

### 5.4.3. Mechanical properties of the scaffolds

The same universal mechanical testing bench equipped with a 100 N load cell was used to evaluate the elastic modulus ( $E$ ) of the scaffolds using uniaxial compression tests. The tests were performed at a crosshead speed of 0.2 mm/min and were aborted when a max extension of 0.3 mm was reached. The stresses and strains were, respectively, calculated based on the ratio of the applied force to the cross-section area and the ratio of the extension to the initial length of the scaffolds in the longitudinal direction. The slope of the first linear region in the stress-strain graph (between 1% and 2% strain) was defined as the  $E$  modulus. The average values with standard deviations are reported ( $n = 3$  for each individual group).

Moreover, we have measured the percentage of the elastic recovery of the crumpled scaffolds after removal of the compressive load under the mentioned conditions ( $n = 3$  in each experimental group). The elastic recovery was calculated by dividing the difference between the length of the crumpled structure before and after removal of the compressive load, by the initial amount of deformation (17 mm).

## 5.5. FEM model

Finite element (FE) simulations were performed using Abaqus (Abaqus 2017, Simulia, US). A dynamic explicit nonlinear solver was used to simulate the crumpling of the cylindrical specimens.

Before setting the simulation parameters, we studied the effect of these parameters on the results of the dynamic explicit simulations (Table S1.). The total mass of the model was artificially increased to reduce the computational time. Based on these initial simulations a mass scaling factor of  $10^6$  and an element size of 0.2 mm were selected, which limits the kinetic energy to < 1% of the internal energy while reducing the computational time by three orders of magnitude. Both the punch and the die were modeled as rigid surfaces and the specimens were discretized using 8042 shell elements (4-node fully integrated).

An elastoplastic material model (von Mises yield function, tabular input of strain hardening data) was used to model the mechanical behavior of Ti. The material model was fitted to the experimental data obtained from the literature [28]. A surface-to-surface contact definition was implemented using a penalty contact enforcement algorithm to capture the contact behavior between the die and specimen as well as the self-contact of the specimen. A friction coefficient of 0.3 was used. The samples were compressed up to 17 mm by adding a displacement boundary condition to the punch.

## 5.6. Morphological characterization

The single-layer crumpled specimens were imaged using a  $\mu$ CT scanner (Phoenix Nanotom, GE Sensing Inspection Technologies GmbH, Germany). The acquisition parameters were: tube current = 230  $\mu$ A, tube voltage = 100 kV, and resolution = 4.5  $\mu$ m  $\times$  4.5  $\mu$ m  $\times$  4.5  $\mu$ m. The acquired data were then reconstructed and saved as DICOM images. The reconstructed data were down-sampled by using a custom-made script in MATLAB (Matlab R2019a). The voxel sizes of the down-sampled scans were: 9  $\mu$ m  $\times$  9  $\mu$ m  $\times$  9  $\mu$ m. Each down-sampled scan was divided into eight regions of interest (ROIs) through the length of the scanned scaffold and was imported into the Dragonfly software (Object Research Systems, Canada). For each ROI, the compressed sheet was segmented using a thresholding technique, and an additional segmentation mask was created based on the smallest cylinder that could cover the entire compressed sheet. The segmented sheet and the cylindrical mask were used in the Bone Analysis plugin of Dragonfly to determine the porosity (%), trabecular thickness (Tb.Th,  $\mu$ m), and pore size (Tb.Sp,  $\mu$ m) of the compressed specimens.

The morphological parameters determined based on the  $\mu$ CT scans were compared to those obtained using FE analyses. Prior to comparison, the deformed specimens were exported from Abaqus to 3-Matic (3-Matic 15.0; Materialise, Leuven, Belgium) in the STL format and were converted into volumes after assigning the compressed specimens a uniform thickness of 125  $\mu$ m and wrapping them (smallest detail: 0.02, protect thin walls and preserve surface structure options are on). The volumes were then divided into 8 ROIs and were post-processed using Dragonfly as described above.

## 5.7. Sample preparation for cell culture

To prepare the 3D nanopatterned Ti samples for cell culture and to access the inner layer (covered with nanopatterns), we uncrumpled the specimens by hand. To remove the PVA coating, the specimens were placed in acetone and water (40 °C) (each for two hours). The specimens were then sterilized in an autoclave at 121 °C for 20 min.

## 5.8. Cell response to the surface

### 5.8.1. Cell seeding and culture

MC3T3-E1 preosteoblast cells (Sigma-Aldrich, Germany) were seeded on the control (polished Ti,  $n = 5$ ) and nanopatterned un-

crumpled specimens ( $n = 5$ ) in a 24 well-plate with a density of 125,000 cells/well. The specimens were incubated in the alpha minimal essential medium ( $\alpha$ -MEM) supplemented with 10% (v/v) fetal bovine serum (FBS) and 1% (v/v) penicillin-streptomycin (all from Thermo Fisher Scientific, US) for 3 or 7 days (37 °C, 5% CO<sub>2</sub>). The culture medium was refreshed every 2–3 days, starting from day 2 of the experiment.

### 5.8.2. Metabolic activity

The metabolic activity of the MC3T3-E1 cells was determined using the PrestoBlue assay (Thermo Fisher Scientific, US) on days 3 and 7. The specimens were transferred into a new 24 well-plate and were incubated in 450  $\mu$ l of fresh culture medium with 50  $\mu$ l of PrestoBlue cell viability reagent for one hour at 37 °C. After incubation, 100  $\mu$ l of the supernatant from each well was transferred to a 96 well plate in duplicate and the fluorescence was measured at an excitation wavelength of 530 nm and an emission wavelength of 595 nm with a Victor X3 microplate reader (PerkinElmer, The Netherlands).

### 5.8.3. Cell viability and SEM imaging

A live/dead cell staining assay (Thermo Fisher Scientific, US) was performed to investigate the viability of the cultured cells after 7 days. The samples were washed 3 times with 10X PBS and were incubated in PBS containing 2  $\mu$ M Calcein AM and 3  $\mu$ M Ethidium homodimer-1 for 30 min at room temperature. After staining, the cells were washed with PBS and were imaged with a fluorescent microscope (ZOE cell imager, Bio-Rad, The Netherlands). Consequently, the stained specimens were fixed with 4% paraformaldehyde (Sigma Aldrich, Germany) for 15 min and were rinsed 2 times with distilled water for 5 min. The samples were then dehydrated in a series of graded ethanol/water solutions (Sigma-Aldrich, Germany) as follows: 15 min in 50%, 20 min in 70%, and 20 min in 96%. The specimens were dried overnight and were gold-sputtered prior to SEM imaging.

### 5.8.4. Image analysis

ImageJ 1.53c (NIH, US) was used to quantify the data from the SEM images. Thereafter, the Analyze Particles command was used to measure the cell aspect ratio by fitting ellipses to the cell body area. Furthermore, the values of the cell area and perimeter were used to calculate the cell shape index as described elsewhere [62].

### 5.9. Statistical analysis

For all of the above-mentioned experiments, the raw data was first tested for normal distribution using the D'Agostino-Pearson omnibus normality test in Prism version 9.1.2 (GraphPad, US). The two-way ANOVA test was performed followed by the Sidak's multiple comparisons test to determine statistical significance of the differences between the means of different groups. A  $p$ -value below 0.05 was considered to indicate statistical significance.

#### Data Availability

The raw data required to reproduce these findings are available to download from (). The processed data required to reproduce these findings are available to download from ().

### Declaration of Competing Interest

The authors declare that they have no known competing financial interests or personal relationships that could have appeared to influence the work reported in this paper.

### Acknowledgments

This research has received funding from the European Research Council under the ERC grant agreement no. [677575]<sup>o</sup>. The authors would like to thank Dr. Françoise Bobbert for preparing the schematic and Dr. Cornelis W. Hagen (Kees) for the access to the SEM equipment.

### Appendix A. Supplementary material

Supplementary data to this article can be found online at <https://doi.org/10.1016/j.matdes.2022.110844>.

### References

- [1] Y. Li, H. Jahr, J. Zhou, A.A. Zadpoor, Additively manufactured biodegradable porous metals, *Acta Biomater.* 115 (2020) 29–50.
- [2] S. Dobbenga, L.E. Fratila-Apachitei, A.A. Zadpoor, Nanopattern-induced osteogenic differentiation of stem cells – a systematic review, *Acta Biomater.* 46 (2016) 3–14.
- [3] K. Modaresifar, M. Ganjian, L. Angeloni, M. Minneboo, M.K. Ghatkesar, P.-L. Hagedoorn, L.E. Fratila-Apachitei, A.A. Zadpoor, On the use of black Ti as a bone substituting biomaterial: behind the scenes of dual-functionality, *Small* 17 (24) (2021) 2100706.
- [4] S.G. Higgins, M. Becce, A. Belessiotis-Richards, H. Seong, J.E. Sero, M.M. Stevens, High-aspect-ratio nanostructured surfaces as biological metamaterials, *Adv. Mater.* 32 (9) (2020) 1903862.
- [5] Y. Yang, K. Wang, X. Gu, K.W. Leong, Biophysical regulation of cell behavior—cross talk between substrate stiffness and nanotopography, *Engineering* 3 (1) (2017) 36–54.
- [6] F. Han, C. Zhu, Q. Guo, H. Yang, B. Li, Cellular modulation by the elasticity of biomaterials, *J. Mater. Chem. B* 4 (1) (2016) 9–26.
- [7] W. Guo, K. Yang, X. Qin, R. Luo, H. Wang, R. Huang, Polyhydroxyalkanoates in tissue repair and regeneration, *Eng. Regen.* 3 (1) (2022) 24–40.
- [8] W. Zhuge, H. Liu, W. Wang, J. Wang, Microfluidic bioscaffolds for regenerative engineering, *Eng. Regen.* 3 (1) (2022) 110–120.
- [9] J. Wang, D. Huang, H. Yu, Y. Cheng, H. Ren, Y. Zhao, Developing tissue engineering strategies for liver regeneration, *Eng. Regen.* 3 (1) (2022) 80–91.
- [10] S.J. Callens, R.J. Uyttendaele, L.E. Fratila-Apachitei, A.A. Zadpoor, Substrate curvature as a cue to guide spatiotemporal cell and tissue organization, *Biomaterials* 232 (2020) 119739.
- [11] D.E. Discher, P. Janmey, Y.-L. Wang, Tissue cells feel and respond to the stiffness of their substrate, *Science* 310 (5751) (2005) 1139–1143.
- [12] A.J. Engler, S. Sen, H.L. Sweeney, D.E. Discher, Matrix elasticity directs stem cell lineage specification, *Cell* 126 (4) (2006) 677–689.
- [13] O. Chaudhuri, L. Gu, D. Klumpers, M. Darnell, S.A. Bencherif, J.C. Weaver, N. Huebsch, H.-P. Lee, E. Lippens, G.N. Duda, D.J. Mooney, Hydrogels with tunable stress relaxation regulate stem cell fate and activity, *Nat. Mater.* 15 (3) (2016) 326–334.
- [14] M. Ganjian, K. Modaresifar, H. Zhang, P.-L. Hagedoorn, L.E. Fratila-Apachitei, A. A. Zadpoor, Reactive ion etching for fabrication of biofunctional titanium nanostructures, *Sci. Rep.* 9 (1) (2019) 1–20.
- [15] M. Ganjian, K. Modaresifar, M.R. Ligeon, L.B. Kunkels, N. Tümer, L. Angeloni, C. W. Hagen, L.G. Otten, P.-L. Hagedoorn, I. Apachitei, L.E. Fratila-Apachitei, A.A. Zadpoor, Nature helps: toward bioinspired bactericidal nanopatterns, *Adv. Mater. Interf.* 6 (16) (2019) 1900640.
- [16] T.L. Clainche, D. Linklater, S. Wong, P. Le, S. Juodkazis, X.L. Guével, J.-L. Coll, E.P. Ivanova, V. Martel-Frchet, interfaces, Mechano-bactericidal titanium surfaces for bone tissue engineering, *ACS Appl. Mater. Interf.* 12 (43) (2020) 48272–48283.
- [17] D.P. Linklater, V.A. Baulin, S. Juodkazis, R.J. Crawford, P. Stoodley, E.P. Ivanova, Mechano-bactericidal actions of nanostructured surfaces, *Nat. Rev.* 19 (1) (2021) 8–22.
- [18] A. Roy, K. Chatterjee, Bactericidal anisotropic nanostructures on titanium fabricated by maskless dry etching, *ACS Appl. Nano Mater.* 5 (3) (2022) 4447–4461.
- [19] S. Hawi, S. Goel, V. Kumar, O. Pearce, W.N. Ayre, E.P. Ivanova, Critical review of nanopillar-based mechanobactericidal systems, *ACS Appl. Nano Mater.* 5 (1) (2022) 1–17.
- [20] L. Yang, L. Ge, Q. Zhou, T. Mokabber, Y. Pei, R. Bron, P. van Rijn, Biomimetic multiscale hierarchical topography enhances osteogenic differentiation of human mesenchymal stem cells, *Adv. Mater. Interf.* 7 (14) (2020) 2000385.
- [21] F.S.L. Bobbert, A.A. Zadpoor, Effects of bone substitute architecture and surface properties on cell response, angiogenesis, and structure of new bone, *J. Mater. Chem. B* 5 (31) (2017) 6175–6192.
- [22] J. Parthasarathy, B. Starly, S. Raman, A design for the additive manufacture of functionally graded porous structures with tailored mechanical properties for biomedical applications, *J. Manuf. Process* 13 (2) (2011) 160–170.
- [23] A.K. Gain, L. Zhang, M.Z. Quadir, Composites matching the properties of human cortical bones: the design of porous titanium-zirconia (Ti-ZrO<sub>2</sub>)

- nanocomposites using polymethyl methacrylate powders, *Mater. Sci. Eng.: A* 662 (2016) 258–267.
- [24] H. Attar, L. Löber, A. Funk, M. Calin, L. Zhang, K. Prashanth, S. Scudino, Y. Zhang, J. Eckert, Mechanical behavior of porous commercially pure Ti and Ti–TiB composite materials manufactured by selective laser melting, *Mater. Sci. Eng.: A* 625 (2015) 350–356.
- [25] M.C. Fokker, S. Janbaz, A.A. Zadpoor, Crumpling of thin sheets as a basis for creating mechanical metamaterials, *RSC Adv.* 9 (9) (2019) 5174–5188.
- [26] M. Meloni, J. Cai, Q. Zhang, D. Sang-Hoon Lee, M. Li, R. Ma, T.E. Parashkevov, J. Feng, Engineering Origami: a comprehensive review of recent applications, design methods, and tools, *Adv. Sci.* 8 (13) (2021) 2000636.
- [27] Z. Zhai, L. Wu, H. Jiang, Mechanical metamaterials based on origami and kirigami, *Appl. Phys. Rev.* 8 (4) (2021) 041319.
- [28] T. van Manen, S. Janbaz, M. Ganjian, A.A. Zadpoor, Kirigami-enabled self-folding origami, *Mater. Today* 32 (2020) 59–67.
- [29] L. Jin, A.E. Forte, B. Deng, A. Rafsanjani, K. Bertoldi, Kirigami-inspired inflatables with programmable shapes, *Adv. Mater.* 32 (33) (2020) 2001863.
- [30] B. Mota, S. Herculano-Houzel, Cortical folding scales universally with surface area and thickness, not number of neurons, *Science* 349 (6243) (2015) 74–77.
- [31] T. Tallinen, J.Y. Chung, F. Rousseau, N. Girard, J. Lefèvre, L.J.N.P. Mahadevan, On the growth and form of cortical convolutions, *Nat. Phys.* 12 (6) (2016) 588–593.
- [32] E. Katzav, M. Adda-Bedia, A. Boudaoud, A statistical approach to close packing of elastic rods and to DNA packaging in viral capsids 103 (50) (2006) 18900–18904.
- [33] S. Deboeuf, E. Katzav, A. Boudaoud, D. Bonn, M. Adda-Bedia, Comparative study of crumpling and folding of thin sheets, *Phys Rev Lett* 110 (10) (2013) 104301.
- [34] J.H. Brackenbury, Wing folding and free-flight kinematics in Coleoptera (Insecta): a comparative study, *J. Zool.* 232 (2) (1994) 253–283.
- [35] N. Kleckner, D. Zickler, G.H. Jones, J. Dekker, R. Padmore, J. Henle, J. Hutchinson, A mechanical basis for chromosome function, *Proc. Natl. Acad. Sci. U.S.A.* 101 (34) (2004) 12592.
- [36] H. Heng, J.W. Chamberlain, X.-M. Shi, B. Spyropoulos, L.-C. Tsui, P.B. Moens, Regulation of meiotic chromatin loop size by chromosomal position, *Proc. Natl. Acad. Sci. U.S.A.* 93 (7) (1996) 2795–2800.
- [37] M. Habibi, M. Adda-Bedia, D. Bonn, Effect of the material properties on the crumpling of a thin sheet, *Soft Matter* 13 (22) (2017) 4029–4034.
- [38] Y.C. Lin, Y.L. Wang, Y. Liu, T.M. Hong, Crumpling under an ambient pressure, *Phys Rev Lett* 101 (12) (2008) 125504.
- [39] K. Matan, R.B. Williams, T.A. Witten, S.R. Nagel, Crumpling a thin sheet, *Phys Rev Lett* 88 (7) (2002) 076101.
- [40] A.D. Cambou, N. Menon, Orientational ordering in crumpled elastic sheets, *EPL (Europhys. Lett.)* 112 (1) (2015) 14003.
- [41] S. Cottrino, P. Viviers, D. Fabrègue, E. Maire, Mechanical properties of crumpled aluminum foils, *Acta Mater.* 81 (2014) 98–110.
- [42] D. Hughes, E.H. Amalu, T. Pak, R. Kennedy, Effect of relative density on compressive load response of crumpled aluminium foil mesh, *Materials* 12 (23) (2019) 4018.
- [43] R. Hedayati, S. Ahmadi, K. Lietaert, B. Pouran, Y. Li, H. Weinans, C. Rans, A.A. Zadpoor, Isolated and modulated effects of topology and material type on the mechanical properties of additively manufactured porous biomaterials, *J. Mech. Behav. Biomed. Mater.* 79 (2018) 254–263.
- [44] A. Higuchi, Q.-D. Ling, Y. Chang, S.-T. Hsu, A. Umezawa, Physical cues of biomaterials guide stem cell differentiation fate, *Chem. Rev.* 113 (5) (2013) 3297–3328.
- [45] M.F. Griffin, P.E. Butler, A.M. Seifalian, D.M. Kalaskar, Control of stem cell fate by engineering their micro and nanoenvironment, *World J. Stem. Cells* 7 (1) (2015) 37.
- [46] X. Chen, H. Fan, X. Deng, L. Wu, T. Yi, L. Gu, C. Zhou, Y. Fan, X. Zhang, Scaffold structural microenvironmental cues to guide tissue regeneration in bone tissue applications, *Nanomaterials* 8 (11) (2018) 960.
- [47] N.E. Fedorovich, E. Kuipers, D. Gawlitza, W.J. Dhert, J. Alblas, Scaffold porosity and oxygenation of printed hydrogel constructs affect functionality of embedded osteogenic progenitors, *Tissue Eng. Part A* 17 (19–20) (2011) 2473–2486.
- [48] M. Miron-Mendoza, J. Seemann, F. Grinnell, The differential regulation of cell motile activity through matrix stiffness and porosity in three dimensional collagen matrices, *Biomaterials* 31 (25) (2010) 6425–6435.
- [49] B. Zhang, X. Pei, C. Zhou, Y. Fan, Q. Jiang, A. Ronca, U. D'Amora, Y. Chen, H. Li, Y. Sun, X. Zhang, The biomimetic design and 3D printing of customized mechanical properties porous Ti6Al4V scaffold for load-bearing bone reconstruction, *Mater. Des.* 152 (2018) 30–39.
- [50] N. Putra, M. Mirzaali, I. Apachitei, J. Zhou, A.A. Zadpoor, Multi-material additive manufacturing technologies for Ti-, Mg-, and Fe-based biomaterials for bone substitution, *Acta Biomater.* 109 (2020) 1–20.
- [51] F.S.L. Bobbert, S. Janbaz, T. van Manen, Y. Li, A.A. Zadpoor, Russian doll deployable meta-implants: fusion of kirigami, origami, and multi-stability, *Mater. Des.* 191 (2020) 108624.
- [52] M.F. Cutiungco, P.M. Reynolds, C.D. Syme, N. Gadegaard, Nanotopography controls single-molecule mobility to determine overall cell fate, *BioRxiv* (2020).
- [53] P. Romani, L. Valcarcel-Jimenez, C. Frezza, S. Dupont, Crosstalk between mechanotransduction and metabolism, *Nat. Rev. Mol. Cell Biol.* 22 (1) (2021) 22–38.
- [54] J. Hasan, S. Jain, K. Chatterjee, Nanoscale topography on black titanium imparts multi-biofunctional properties for orthopedic applications, *Sci. Rep.* 7 (2017) 41118.
- [55] S. Oh, K.S. Brammer, Y.J. Li, D. Teng, A.J. Engler, S. Chien, S. Jin, Stem cell fate dictated solely by altered nanotube dimension, *Proc. Natl. Acad. Sci. U.S.A.* 106 (7) (2009) 2130–2135.
- [56] S. Watari, K. Hayashi, J.A. Wood, P. Russell, P.F. Nealey, C.J. Murphy, D.C. Genetos, Modulation of osteogenic differentiation in hMSCs cells by submicron topographically-patterned ridges and grooves, *Biomaterials* 33 (1) (2012) 128–136.
- [57] G. Kumar, C.K. Tison, K. Chatterjee, P.S. Pine, J.H. McDaniel, M.L. Salit, M.F. Young, C.G. Simon Jr, The determination of stem cell fate by 3D scaffold structures through the control of cell shape, *Biomaterials* 32 (35) (2011) 9188–9196.
- [58] G. Nardone, J. Oliver-De La Cruz, J. Vrbsky, C. Martini, J. Pribyl, P. Skládal, M. Pešl, G. Caluori, S. Pagliari, F. Martino, Z. Maceckova, M. Hajduch, A. Sanz-García, N. Maria Pugno, G. Bernard Stokin, G. Forte, YAP regulates cell mechanics by controlling focal adhesion assembly, *Nat. Commun.* 8 (1) (2017) 1–13.
- [59] Y. Hou, W. Xie, L. Yu, L.C. Camacho, C. Nie, M. Zhang, R. Haag, Q. Wei, Surface roughness gradients reveal topography-specific mechanosensitive responses in human mesenchymal stem cells, *Small* 16 (10) (2020) 1905422.
- [60] K. Cai, J. Bossert, K.D. Jandt, Does the nanometre scale topography of titanium influence protein adsorption and cell proliferation?, *Colloids Surf, B* 49 (2) (2006) 136–144.
- [61] D. Khang, J. Choi, Y.-M. Im, Y.-J. Kim, J.-H. Jang, S.S. Kang, T.-H. Nam, J. Song, J.-W. Park, Role of subnano-, nano- and submicron-surface features on osteoblast differentiation of bone marrow mesenchymal stem cells, *Biomaterials* 33 (26) (2012) 5997–6007.
- [62] S. Park, H.-H. Park, K. Sun, Y. Gwon, M. Seong, S. Kim, T.-E. Park, H. Hyun, Y.-H. Choung, J. Kim, Hydrogel nanospine patch as a flexible anti-pathogenic scaffold for regulating stem cell behavior, *ACS Nano* 13 (10) (2019) 11181–11193.